Electronic Supplementary Material (ESI) for Journal of Materials Chemistry A.


# Supporting Information

# A multichannel photothermal rod for antigravity water transportation and high-flux solar steam generation

Chenyang Dang[1], Meihua Chen[1], Lin Huang[1], Mingming Chu[1], Yiming Li[1,*], Lujia Liu[1,2*] and Xuebo Cao[1,*]

[1] College of Biological, Chemical Sciences and Engineering, Jiaxing University, Jiaxing, Zhejiang 314001, China

[2] MacDiarmid Institute for Advanced Materials and Nanotechnology, School of Chemical and Physical Sciences, Victoria University of Wellington, Wellington 6012, New Zealand

*e-mail: xbcao@zjxu.edu.cn; liyiming@zjxu.edu.cn; luke.liu@vuw.ac.nz

This file includes:

**Table S3.** Distribution of radii for the MCPR channels and pumping static height calculation.

**Movie S1.** Video displaying the water transport properties of the VCA & HCA structure and single VCA structure.

**Movie S2.** Video displaying the water pumping properties of the MCPR and the carbonized balsa wood.

**Note S1.** Characterizations in details.

**Table S1. Summary of representative references on solar-driven evaporation**

| Refs | Evaporation rate (kg $m^{-2}$ $h^{-1}$) | Evaporation rate (kg $m^{-2}$ $day^{-1}$) | Required area ($m^2$)* |
|---|---|---|---|
| This work | 18.8 (Lab) | 150.4 | 3.99 |
| | 34 (Outdoor) | 272 | 2.2 |
| | 126.5 (Outdoor) | 1012 | 0.6 |
| 1 | 1.2 | 9.6 | 62.50 |
| 2 | 1.26 | 10.08 | 59.52 |
| 3 | 2.7 | 21.6 | 27.78 |
| 4 | 1.96 | 15.68 | 38.27 |
| 5 | 2 | 16 | 37.50 |
| 6 | 2.5 | 20 | 30.00 |
| 7 | 3.6 | 28.8 | 20.83 |
| 8 | 2.63 | 21.04 | 28.52 |
| 9 | 3.2 | 25.6 | 23.44 |
| 10 | 2.3 | 18.4 | 32.61 |
| 11 | 1.94 | 15.52 | 38.66 |
| 12 | 2.25 | 18 | 33.33 |
| 13 | 1.25 | 10 | 60.00 |
| 14 | 1.95 | 15.6 | 38.46 |
| 15 | 2.045 | 16.36 | 36.67 |
| 16 | 2.09 | 16.72 | 35.89 |
| 17 | 1.32 | 10.56 | 56.82 |
| 18 | 1.57 | 12.56 | 47.77 |
| 19 | 1.7 | 13.6 | 44.12 |
| 20 | 1.26 | 10.08 | 59.52 |
| 21 | 2.2 | 17.6 | 34.09 |
| 22 | 1.04 | 8.32 | 72.12 |
| 23 | 1.56 | 12.48 | 48.08 |
| 24 | 1.42 | 11.36 | 52.82 |
| 25 | 1.475 | 11.8 | 50.85 |
| 26 | 2.23 | 17.84 | 33.63 |
| 27 | 10.9 | 87.2 | 6.88 |
| 28 | 3.824 | 30.592 | 19.61 |
| 29 | 2.99 | 23.92 | 25.08 |
| 30 | 2.94 | 23.52 | 25.51 |
| 31 | 5.15 | 41.2 | 14.56 |
| 32 | 2.35 | 18.8 | 31.91 |
| 33 | 2.17 | 17.36 | 34.56 |
| 34 | 7.6 | 60.8 | 9.87 |

| | | | |
|---|---|---|---|
| 35 | 2.5 | 20 | 30 |
| 36 | 4.12 | 32.96 | 18.2 |
| 37 | 4.1 | 32.8 | 18.29 |
| 38 | 4.2 | 33.6 | 17.86 |
| 39 | 3.6 | 28.8 | 20.83 |
| 40 | 3.05 | 24.4 | 24.59 |
| 41 | 3.72 | 29.76 | 20.16 |
| 42 | 2.43 | 19.44 | 30.86 |
| 43 | 3.17 | 25.36 | 23.66 |
| 44 | 3.62 | 28.96 | 20.72 |
| 45 | 4.02 | 32.16 | 18.66 |
| 46 | 2.317 | 18.536 | 32.37 |
| 47 | 2.32 | 18.56 | 32.33 |
| 48 | 2.42 | 19.36 | 30.99 |
| 49 | 3.65 | 29.2 | 20.55 |
| 50 | 3.23 | 25.84 | 23.22 |
| 51 | 3.2 | 25.6 | 23.44 |
| 52 | 2.25 | 18 | 33.33 |
| 53 | 2.8 | 22.4 | 26.79 |
| **Mean** | **~ 2.81** | **~ 22.53** | **~ 32.8** |

***** Take the daily water consumption of a family of four as an example, assuming that the sun is fully irradiated for 8 h a day. According to statistics from the UK water sector and the ministry of water resources of China, the daily water consumption per capita is 150 and 157 liters, respectively. Assuming that the daily water consumption of a family of four is 600 liters, and the fresh water produced by the the photothermal evaporation device is used to meet this daily water demand, the required irradiation area can be calculated by the following formula (1)：

$$S = (n \cdot m)/(\eta \cdot t) \quad (1)$$

where $S$ ($m^2$) is the required irradiation area, n is number of people, m (kg $day^{-1}$ or L $day^{-1}$) is the daily water consumption per capita, $\eta$ (kg $m^{-2}$ $h^{-1}$) is the photothermal evaporation efficiency of the SDE system, $t$ (h) is the time that the sun is sufficiently irradiated in a day.

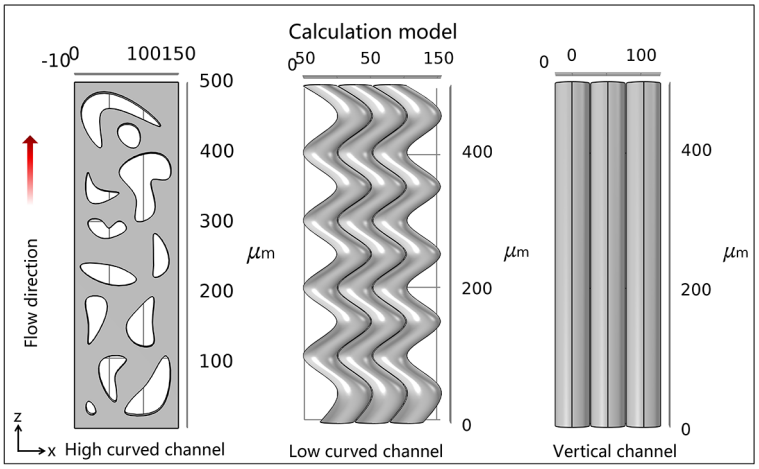


**Figure S1. The computational domain used in the CFD simulation to determine water diffusion through the rod-like photothermal materials.**

**Computational Fluid Dynamics (CFD) modeling: Fluid Diffusion.** COMSOL multiphysics software was used to understand the diffusion of fluid in photothermal materials with different internal structures. For rod-like photothermal materials we have assumed three different microstructures. Different water diffusion path structures were constructed by adjusting the internal tortuosity of the photothermal material. The evaporation rate on the model top is taken from the standard AM1.5G photothermal conversion efficiency with 100% (set at 4.425 μm $s^{-1}$), while the bottom fluid region was set at a constant hydrostatic pressure. Under the condition of fixed exit velocity, the flow resistance of the fluid in the photothermal material was investigated through the change of shear rate (**Figure 1b**). In addition, the change of fluid flow rate was also explored under the condition of constant inlet pressure (10 Pa) (**Figure 1c**). Since the flow rate is very slow, the very low Reynolds number, throughout the microstructure allows us to use a laminar flow model for fluid flow analysis. Note that the flow is considered to be steady and incompressible. Therefore, in the CFD, the COMSOL multiphysics simulation solves the Navier-Stokes equations for steady, incompressible, laminar flow:

$$\rho(\mathbf{u}\cdot\nabla)\mathbf{u} = \nabla\cdot[-p\mathbf{I} + \mu(\nabla\mathbf{u} + (\nabla\mathbf{u})^{T})] + \mathbf{F} + \rho g, \quad (2)$$

$$\rho\nabla\cdot\mathbf{u} = 0 \quad (3)$$

where **u** is the flow velocity vector, $p$ is the pressure, g is the gravity vector, T is fluid temperature (293.15 K), ρ and $\mu$ are the density and the dynamic viscosity of water, respectively.

The simulated data is visualized in **Figure 1b-c** of the main text. The results show that the reduction of the internal tortuosity of the material will reduce the shear rate during fluid diffusion and increase the flow velocity. According to Fick's first law of diffusion；

$$J = D\cdot\mathcal{E}\cdot\nabla c/\tau \quad (4)$$

Where $J$ is diffusion flux, D is diffusion coefficient or diffusivity, Ɛ is the material porosity, c (for ideal mixtures) is the concentration, of which the dimension is amount of substance per unit volume, τ is the tortuosity of the aperture. Fick's first law states that the internal tortuosity of the material is inversely proportional to the diffusion flux, which is consistent with our simulation results.

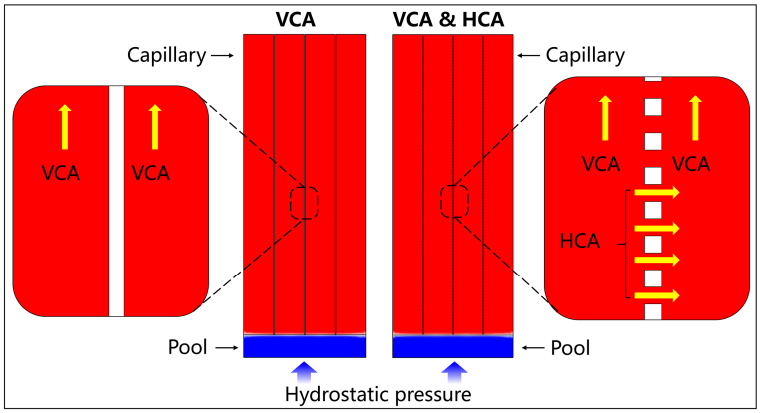


**Figure S2. The computational model of VCA and VCA & HCA used in the CFD simulation to determine water diffusion.**

**CFD modeling: Capillary Filling.** The model consists of a capillary channel of width 0.2 mm attached to a water reservoir. Water can flow freely into the pool. Initially, the capillary channel is filled with air. Wall adhesion causes water to creep up along the capillary channel boundaries. The deformation of the water surface induces surface tension at the air/water interface, which in turn creates a pressure jump across the interface. The pressure variations cause water and air to move upward. The fluids continue to rise until the capillary forces are balanced by the gravity force building up as the water rises in the channel. Two different capillary filling models were constructed: (1) Capillary with vertical channel arrays (VCA); (2) Capillary with vertical and horizontal channel arrays (VCA & HCA).

The Navier-Stokes equations describe the transport of mass and momentum for fluids of constant density. In order to account for capillary effects, it is crucial to include surface tension in the model. The Navier-Stokes equations are then:

$$\rho(\partial\mathbf{u}/\partial t) + \rho(\mathbf{u}\cdot\nabla)\mathbf{u} = \nabla\cdot[-p\mathbf{I} + \mu(\nabla\mathbf{u} + (\nabla\mathbf{u})^{T})] + \mathbf{F}_{st} + \rho g, \quad (5)$$

$$\nabla\cdot\mathbf{u} = 0 \quad (6)$$

Here, $\rho$ denotes the water density, $\mu$ equals the water dynamic viscosity, $\mathbf{u}$ represents the velocity, $p$ denotes the pressure, and g is the gravity vector. $\mathbf{F}_{st}$ is the surface tension force acting at the air/water interface. The diffuse interface representation makes it possible to compute the surface tension by

$$\mathbf{F}_{st} = G\nabla\phi \quad (7)$$

$$G = \lambda[-\nabla^2\phi + \phi(\phi^2-1)/\mathcal{E}^2] \quad (8)$$

where $\phi$ is the phase field parameter, $\lambda$ is the mixing energy density and $\mathcal{E}$ is the interface thickness parameter, and G is the chemical potential.

In the model the two-phase flow dynamics is governed by a Cahn-Hilliard equation. The equation tracks a diffuse interface separating the immiscible phases. When solved in COMSOL Multiphysics, the Cahn-Hilliard equation is split up into two equations:

$$(\partial\mathbf{u}/\partial t) + \mathbf{u}\cdot\nabla\phi = \nabla\cdot(\gamma\lambda/\mathcal{E}^2)\nabla\psi \quad (9)$$

$$\psi = -\nabla\cdot\mathcal{E}^2\nabla\phi + (\phi^2-1)\phi \quad (10)$$

where $\gamma$ is the mobility, the $\psi$ variable is referred to as the phase field help variable. The following equation relates the mixing energy density and the interface thickness to the surface tension coefficient:

$$\sigma = (8/9)^{0.5}\cdot(\lambda/\mathcal{E}) \quad (11)$$

The interface thickness parameter to $\varepsilon = h_c/2$, where $h_c$ is the characteristic mesh size in the region passed by the interface. The mobility parameter $\gamma$ determines the time scale of the Cahn-Hilliard diffusion and the default value, $\gamma=\varepsilon^2$.

The hydrostatic pressure, $p = \rho gz$, gives the pressure at the inflow boundary. The pressure boundary condition

automatically compensates for hydrostatic pressure so the actual value for the pressure is set to zero. At the outlet, the pressure is equal to zero, that is, equal to the pressure at the top of the inflow boundary. The Wetted Wall feature is suitable for solid walls in contact with a fluid interface. It sets the velocity component normal to the wall to zero, and adds a frictional boundary force;

$$F_{fr} = -\mu \mathbf{u}/\beta \tag{12}$$

Here, β is the slip length. The boundary condition also allows to specify the contact angle θ, in this model, the contact angle is 71°.

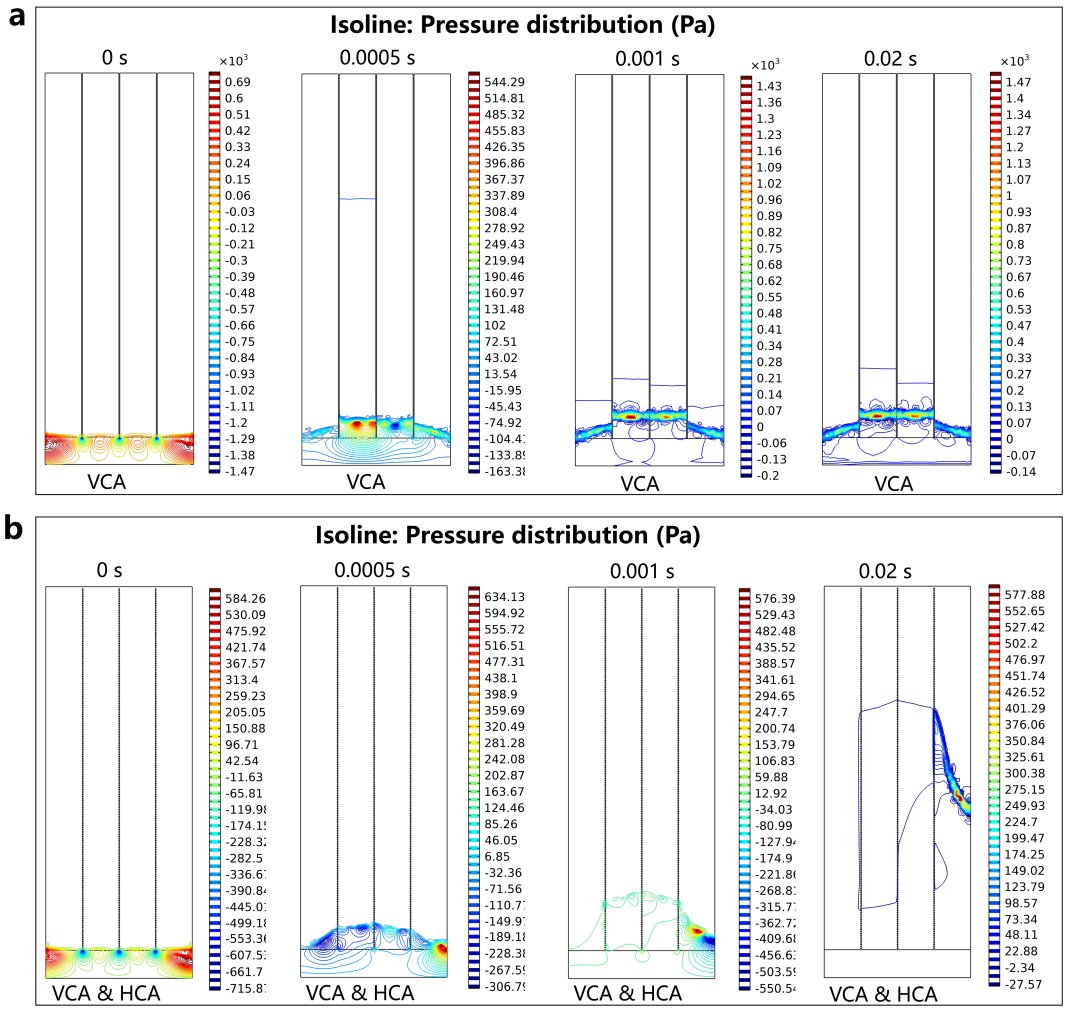


**Figure S3. The pressure distribution of the fluid as it diffuses in the VCA and VCA & HCA structures.** (**a**) VCA. **(b)** VCA & HCA.

The model calculation in **Figure S2** shows that the diffusion height of VCA is only 0.13 mm, while the diffusion height of VCA & HCA can reach 1.36 mm (**Movie S1**). There are two main reasons that the diffusion height of VCA & HCA far exceeds that of VCA (up to 10 times that of VCA). On the one hand, HCA increases the porosity in the system, and the increase in porosity according to the Fick's first law of diffusion (Equation 4) will increase the diffusion flux. On the other hand, it can be clearly seen from **Figure S3** that at the same diffusion time, the pressure that the fluid diffuses in the VCA & HCA structure is smaller than that of the VCA structure. In other words, the existence of HCA balances the pressure when the VCA diffuse the fluid, therefore the fluid can be diffused longer distances under the condition of overcoming gravity.

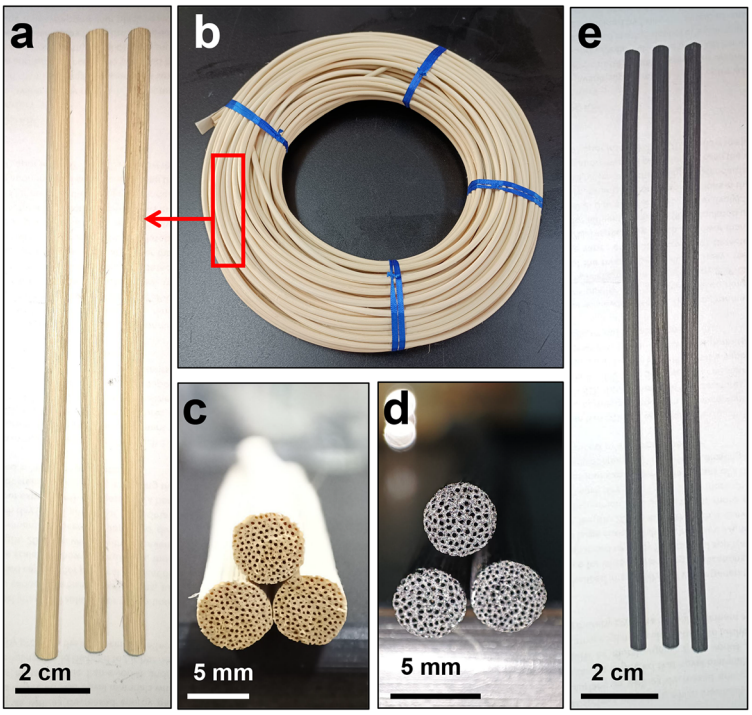


**Figure S4. The appearance of natural rattan before and after carbonization. (a-c)** before carbonization. **(d), (e)** after carbonization.

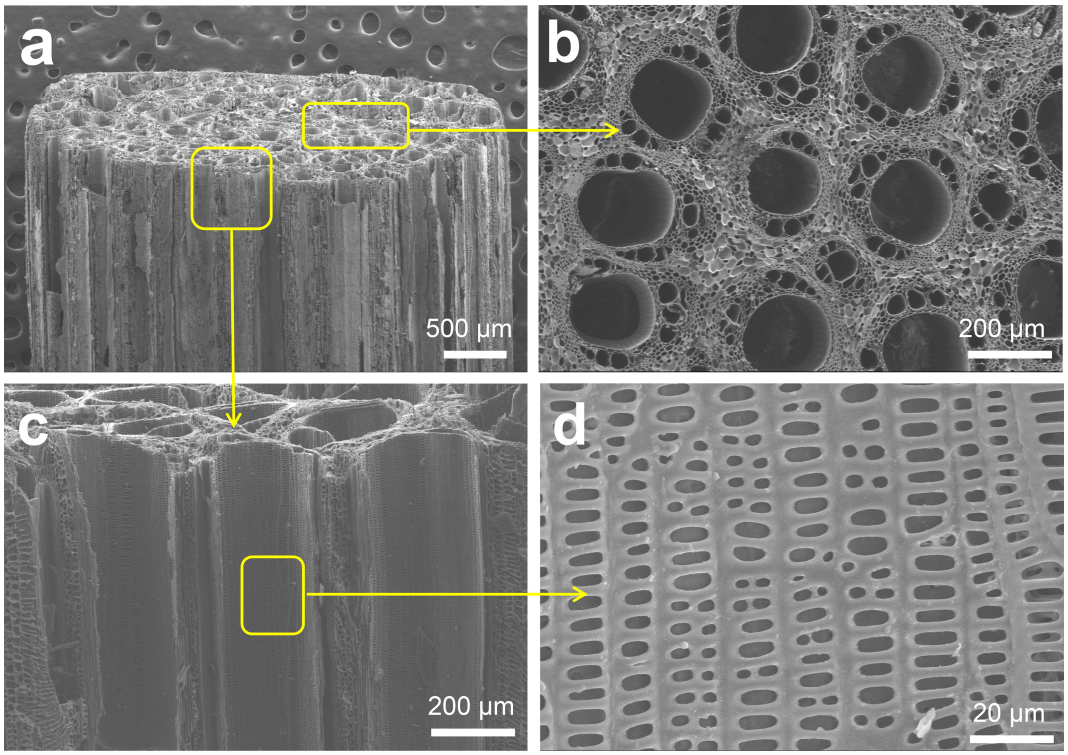


**Figure S5. Microstructure of the MCPR. (a)** Panoramic view of the terminal of the MCPR. **(b)** Top view of the MCPR. **(c), (d)** Side view of the MCPR.

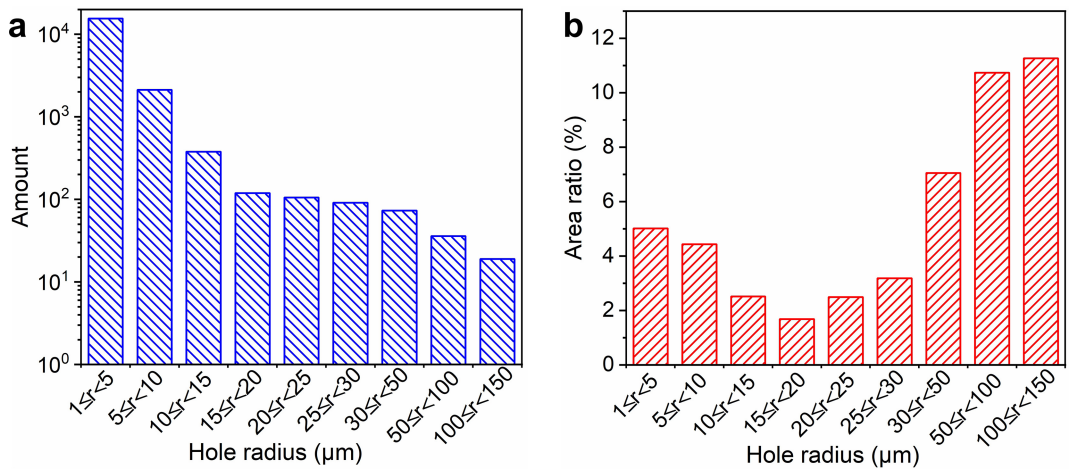


**Figure S6. (a)** Statistics on the size distribution of the channels. **(b)** The ratio of the area of channels with different apertures to the area of all channels.

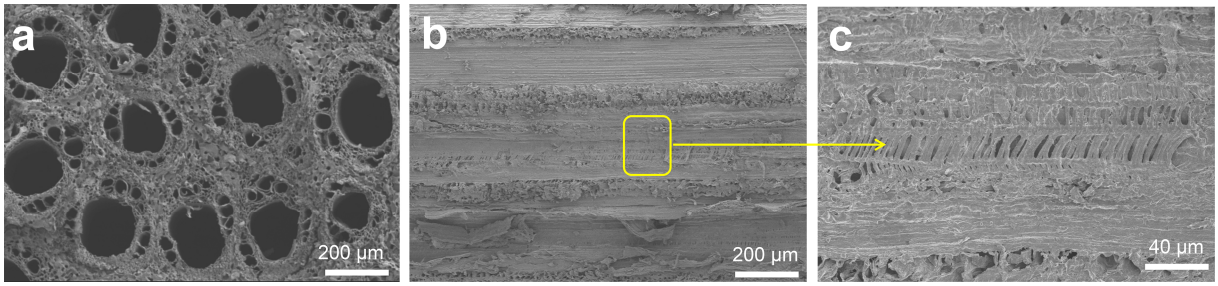


**Figure S7. SEM images for the MCPR containing mainly VCA structure. (a)** Top view of the MCPR showing the presence of vertical channels. **(b, c)** Side views of the MCPR showing that the periodically aligned holes (HCA) are scarce. This VCA-structured MCPR was prepared through a strategy identical to the preparation of VCA&HCA structured MCPR except the simplification of the delignification procedure.

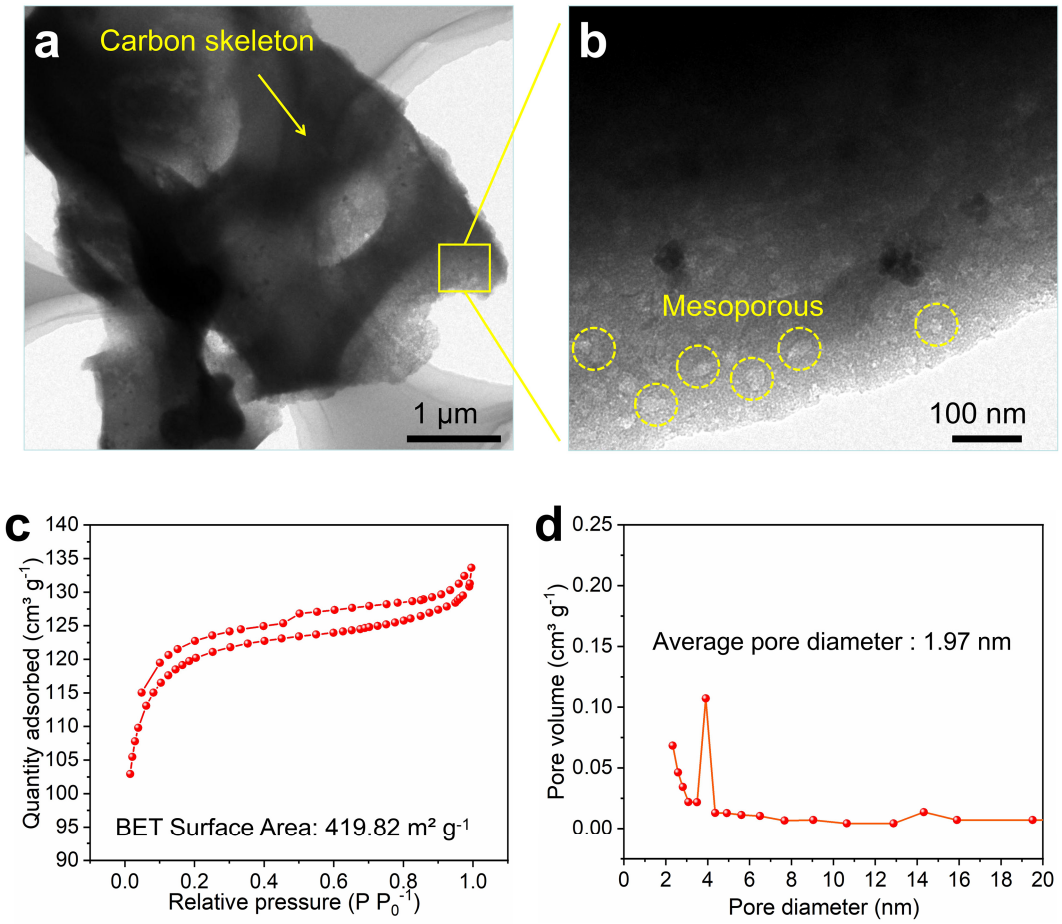


**Figure S8. TEM image of the microscopic morphology, the specific surface area and pore size distribution of the MCPR. (a)** Transmission electron microscopy (TEM) image showing microscopic morphology of carbon skeleton of the MCPR**. (b)** High-magnification TEM image showing the presence of large number of mesopores distributed on the carbon skeleton. **(c)** $N_2$ adsorption-desorption isotherms of MCPR. The specific surface area of the MCPR reaches 419.82 $m^2$ $g^{-1}$. **(d)** Average pore size distribution of MCPR.

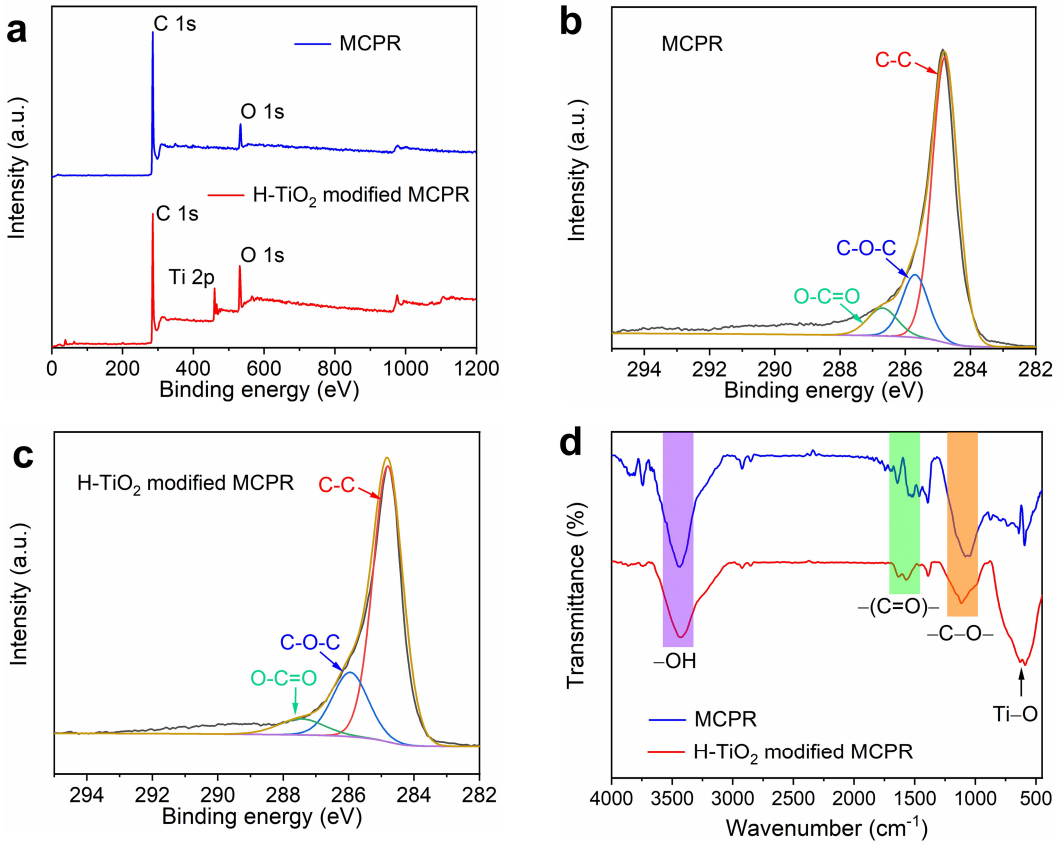


**Figure S9. Chemical characterization of the MCPR with and without $TiO_2$ modification. (a)** Survey XPS spectra of the MCPR. **(b, c)** High-resolution XPS spectra of C 1s in the MCPR. **(d)** FTIR spectra of the MCPR.

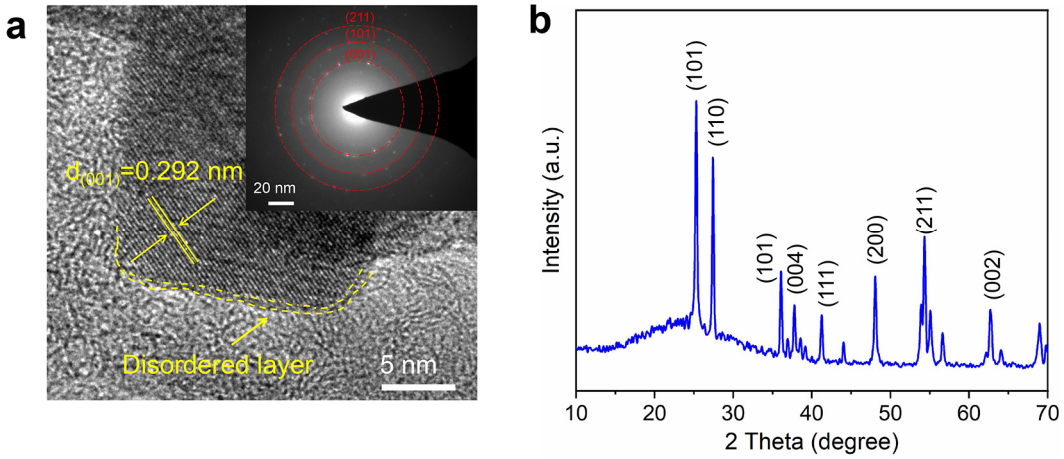


**Figure S10. Structural analysis of H-$TiO_2$ needle by TEM and X-ray diffraction (XRD). (a)** High resolution TEM image of the H-$TiO_2$ needle. Inset shows the corresponding selected area electron diffraction (SAED) pattern. H-$TiO_2$ needle has a polycrystalline structure in rutile phase, which can also be confirmed from the electron diffraction pattern and XRD data. Due to $H_2$ treatment, a thin disordered layer (thick ~1 nm, marked by yellow dotted line) is produced on the surface of the $TiO_2$ crystal. **(b)** XRD data of $TiO_2$ needles.

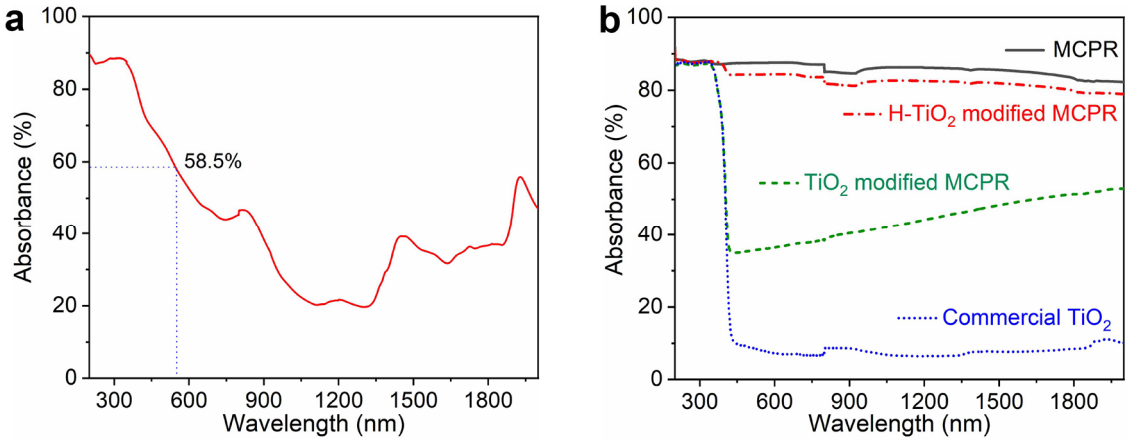


**Figure S11. UV-Vis-NIR absorption spectrum of MCPR and rattan sample. (a)** Natural rattan**. (b)** MCPR, $TiO_2$ modified MCPR, H-$TiO_2$ modified MCPR, and commercial $TiO_2$.The light absorption of natural strips at 550 nm is only 58.5%, and the absorption effect on infrared light with higher wavelengths is worse. In contrast, MCPR shows excellent absorbance in a wide range of wavelengths.

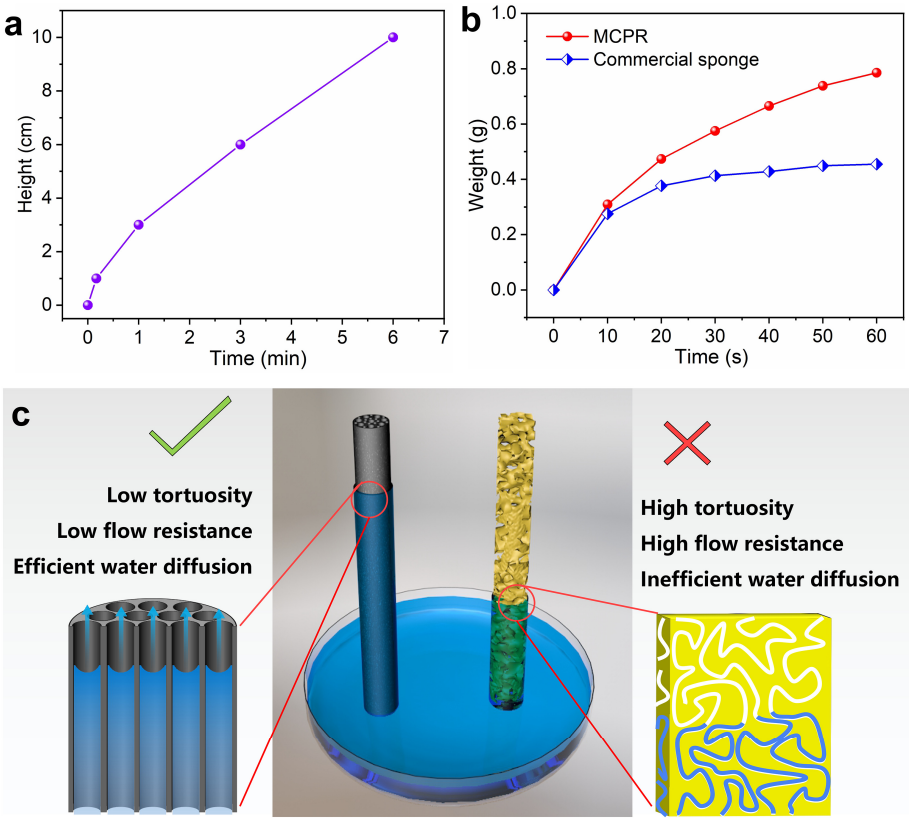


**Figure S12. The water transport property of the MCPR. (a)** Relationship between the pumping height of the MCPR and the time**. (b)** Water absorption capacity of MCPR and commercial sponge at the same volume**. (c)** Water absorption mechanism of MCPR and commercial sponge. The large vertical channel structure of the MCPR has low tortuosity and low water diffusion resistance, so it has high water diffusion performance.

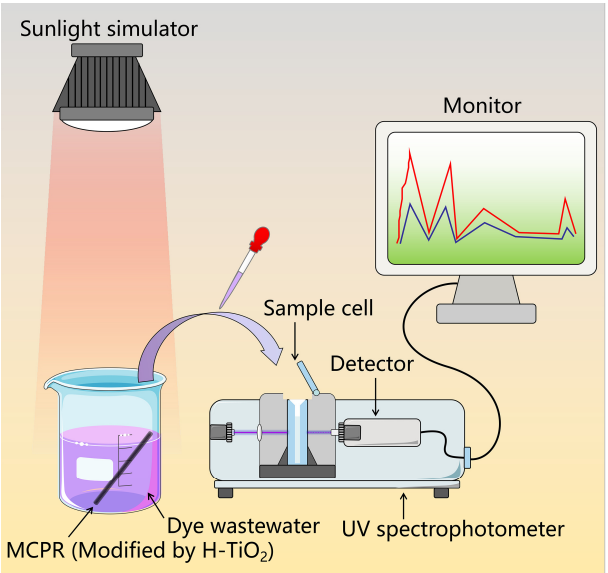


**Figure S13. Assessment of the photocatalytic performance of the MCPR.** MCPR was immersed in the dye wastewater, and the absorbance of the dye wastewater was measured. The samples were taken before light, after light protection overnight, and after exposure to light for 1 h.

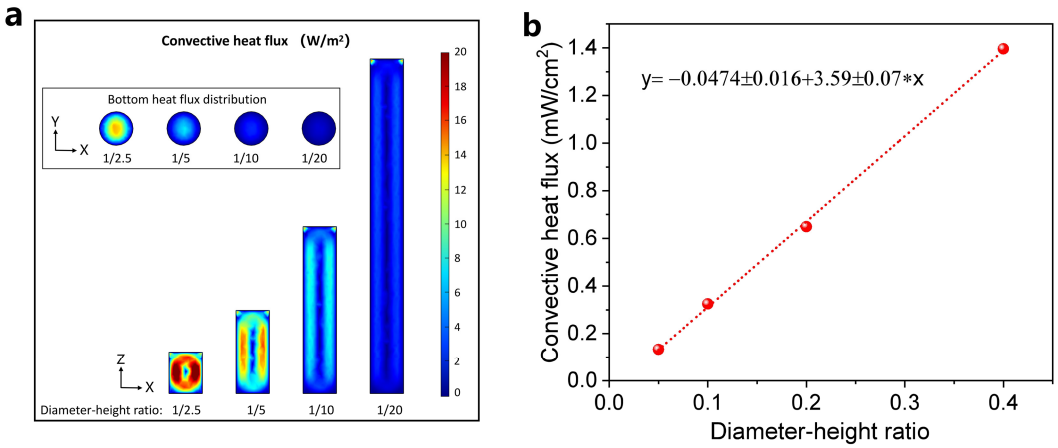


**Figure S14. (a) The internal heat diffusion distribution of models with different diameter-height ratios. (b) Fitting relationship between diameter-height ratio and convective heat flux.**

Compared with the carbon matrix, due to the high specific heat of water and the ability to transfer energy through convection, here we use a fluid heat transfer model to compare the thermal insulation performance of systems at different heights. The heat transfer of carbon, titanium dioxide and other substrates and the energy interaction generated by photocatalysis are ignored. The Boussinesq term defines a force dependent on the temperature and the fluid velocity transports heat. Introduce the Boussinesq term to solve the incompressible Navier-Stokes equations.

$$\rho(\mathbf{u} \cdot \nabla)\mathbf{u} = -\nabla p + \nabla \cdot \mu(\nabla \mathbf{u} + (\nabla \mathbf{u})^{T}) + \rho g \alpha_p (T - T_0), \quad (13)$$

$$\nabla \cdot \mathbf{u} = 0, \quad (14)$$

Where the dependent variables for flow are **u**, the vector of fluid velocity, and p is pressure. $T$ represents photothermal temperature, refer to the highest temperature of the top of the photothermal material under 1 kW $m^{-2}$ solar intensity, about 45 ℃. $T_0$ is a reference bulk water temperature (20 ℃), $g$ denotes gravity acceleration, ρ gives the water reference density. $\mu$ is the dynamic viscosity of water, and $\alpha_p$ equals the coefficient of volumetric thermal expansion.

The heat balance comes from the conduction-convection equation.

$$\rho C_P \mathbf{u} \cdot \nabla T - \nabla \cdot (k \nabla T) = 0 \quad (15)$$

Where $k$ is the thermal conductivity, and $C_p$ is the specific heat capacity of the water. For the Navier-Stokes equations, impermeable, no-slip boundary conditions apply. The no-slip condition results in zero velocity at the wall, with pressure within the domain adopts fixed point constraints.

The model addresses a wide range of cavity sizes, fluid properties, and temperature drops using material properties set up with nondimensional Rayleigh and Prandtl numbers. The Rayleigh number (Ra) gives the ratio of buoyant to viscous forces. The Prandtl number (Pr) gives the ratio of kinematic viscosity to thermal diffusivity.

$$\mathrm{Ra} = (C_p \rho^2 g \alpha_p T L^3) / (\mu k) \quad (16)$$

$$\mathrm{Pr} = (\mu C_p / k) \quad (17)$$

Here L is the length of a side wall.

Setting the body force in the z-direction for the momentum equation (Equation 6), and the fluid properties to $C_p$ = Pr, and ρ = $\mu$ = $k$ = 1, produces a set of equations with nondimensional variables $p$, **u**, and $T$ to solve the Navier-Stokes equations.

$$F_z = (\mathrm{Ra} / \mathrm{Pr})(T - T_c) \quad (18)$$

According to the fitted equation, the heat flux of the MCPR model with a height of 10 cm is as low as ~0.0962 mW $cm^{-2}$, so the system has excellent thermal insulation performance.

**Table S2**

The sewage vaporization enthalpy ($h_{LV}$) was estimated via a control experiment. The sewage samples was set in a closed container under a 25℃ and ambient air pressure. To avoid interference by sensible heat, it is necessary to carefully control the experimental humidity, thereby suppressing the temperature changes caused by rapid evaporation. The $h_{LV}$ of sewage samples can be calculated by using the following formula:

$$E_{in} = \Delta h_0 \times M_0 = \Delta h_{LV} \times M_1 \quad (19)$$

where $E_{in}$ is the identical power input of all samples, $\Delta h_0$ is the vaporization enthalpy of pure water, $\Delta h_0$ changes under different temperature and their relationship can be described by formula 20:

$$h_0 = \alpha + \beta T + \gamma T^{1.5} + \delta T^{2.5} + \varepsilon T^3 \quad (20)$$

where $\alpha$ = 2500.304, $\beta$ = -2.2521025, $\gamma$ = -0.021465847, $\delta$ = $3.1750136\times10^{-4}$ , $\varepsilon$ = $-2.8607959\times10^{-5}$ are constants, and $T$ is temperature (°C). $M_0$ is the evaporation rate of pure water, $\Delta h_{LV}$ is the vaporization enthalpy of sewage sample, and $M_1$ is the evaporation rate of sewage sample. The obtained $h_{LV}$ is used for subsequent calculations of the photothermal conversion efficiency (η) of MCPR evaporators. Using the method proposed by Zhu et al for calculating the energy conversion efficiency of 3D system [54,55], we can evaluate the energy efficiency of MCPR evaporators by taking account into energy input by the environment in addition to vertical sun illumination.

We define the 3D system energy conversion efficiency as:

$$\eta = P_{eva} / (P_{solar} + P_{amb}) \quad (21)$$

where $P_{eva}$ (kJ $m^{-2}$ $h^{-1}$) is the energy absorbed by water evaporation, $P_{solar}$ (kJ $m^{-2}$ $h^{-1}$) is the energy input by direct sunlight, and $P_{amb}$ (kJ $m^{-2}$ $h^{-1}$) is the energy input by the environment.

The Peva can be obtained via the following equation:

$$P_{eva} = \dot{m} \times (h_{LV} + c\Delta T) \quad (22)$$

where $\dot{m}$ (kg $m^{-2}$ $h^{-1}$) is the evaporation rate of the 3D system, $h_{LV}$ (kJ $kg^{-1}$) is the vaporization enthalpy of water, $c$ is the specific heat of water, $\Delta T$ is the temperature difference between the initial bulk water and the evaporating surface.

The $P_{solar}$ can be obtained via the following equation:

$$P_{solar} = C_{opt} \times q \quad (23)$$

where $C_{opt}$ is the optical concentration, $q$ is the nominal solar irradiation.

The $P_{amb}$ can be obtained via the following equation:

$$P_{amb} = P_{sca} + P_{con} \quad (24)$$

$$P_{sca} = C_{opt} \times q_{sca} \quad (25)$$

$$P_{con} = v \times S_l \times h_{LV} \times \rho_{wa} (\phi_s - \phi_{in}) / S_p \text{[27,56,57]} \quad (26)$$

where $P_{sca}$ is the scattered/diffuse reflection light input energy in the ambient, $P_{con}$ is the ambient convection energy input, $q_{sca}$ is the scattered/diffuse reflection solar irradiation (50~200 W $m^{-2}$, depending on the height of the evaporation system.). The $v$ (m $s^{-1}$) denotes the intensity of incoming convective flow ($v$ fluctuates between 0.2~1 m $s^{-1}$, depending on the turbulence of the air by the height of the evaporator), $S_l$ and $S_p$ are the areas of longitudinal section and projection plane of the 3D system, respectively. The $\rho_{wa}$ (kg $m^{-3}$) is the density of wet air. $\phi_s$ and $\phi_{in}$ represent the humidity ratios of saturated wet air and incoming convective flow, respectively.

The evaporative tests for this work were performed under a temperature of 20±1 ℃ and humidity of 45±5% RH. The energy conversion efficiencies for the 3D evaporators with various heights are summarized in the following **Table S2**.

**Table S2. Summary of the energy conversion efficiency.**

| Evaporator height (cm) | 0.1 | 1 | 4 | 10 |
|---|---|---|---|---|

| | | | | |
|---|---|---|---|---|
| Evaporation rate (kg $m^{-2}$ $h^{-1}$) | 1.83 | 9.07 | 15.6 | 18.8 |
| Energy input by direct sunlight $P_{solar}$ (kJ $m^{-2}$ $h^{-1}$) | 3600 | 3600 | 3600 | 3600 |
| Energy input by the environment $P_{amb}$ (kJ $m^{-2}$ $h^{-1}$) | * | 42822.88 | 168815.91 | 421356.61 |
| Energy absorbed by water evaporation $P_{eva}$ (kJ $m^{-2}$ $h^{-1}$) | 3171.02 | 15337.3 | 26379.6 | 31790.8 |
| System efficiency (apparent) | 88% | 439% | 755% | 910% |
| System efficiency (contains ambient energy) | 88% | 33.03% | 15.30% | 7.48% |

* The 0.1 cm height evaporator approaches the 2D system ignoring the input of ambient energy.

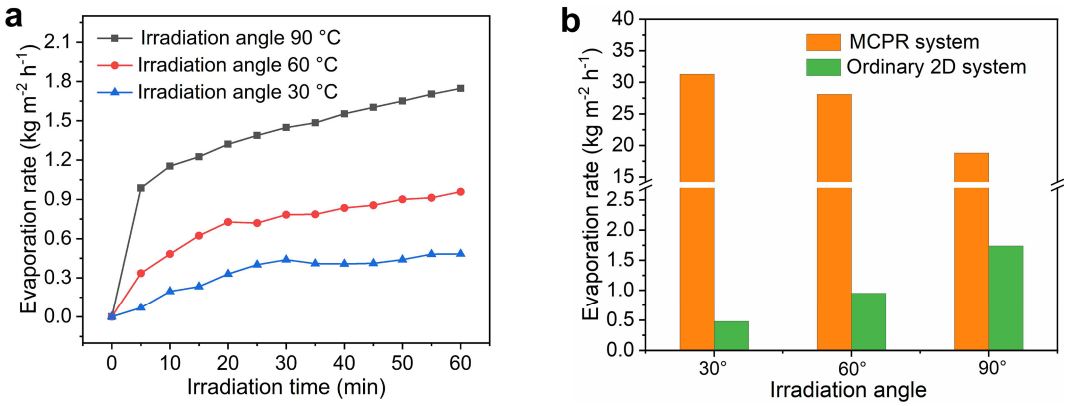


**Figure S15. The evaporation rate of MCPR system and 2D system under different irradiation angles. (a)** Evaporation rates of the 2D system irradiated by 1 sun from 30°, 60°, and 90°. **(b)** Comparison of MCPR system and 2D system. Note: The 2D system is constructed by adjusting the height of the 3D MCPR system protruding from the water surface to 0 cm, and all other preparation parameters are consistent with the 3D system.

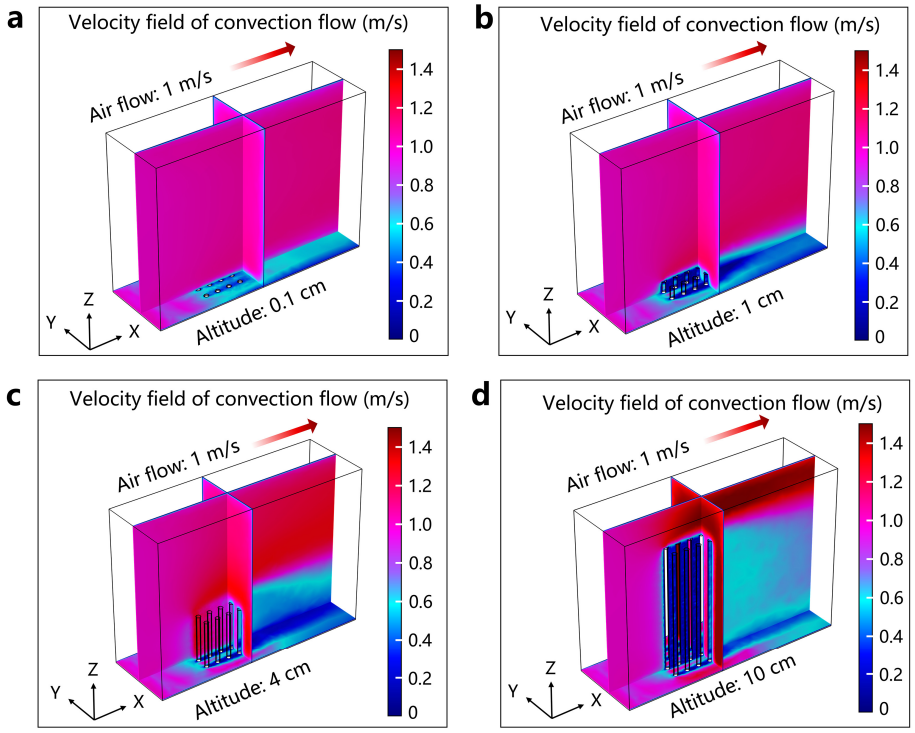


**Figure S16. Effect of evaporators with different heights on air turbulence. (a)** Altitude 0.1cm. **(b)** Altitude 1 cm. **(c)** Altitude 4 cm. **(d)** Altitude 10 cm.

**CFD modeling: Air convection and transport of moisture in the air.** An array of evaporators with different heights (0.1, 1, 4, 10 cm) was constructed, and the influence of moisture transmission caused by air turbulence was explored. Considering that the increase in the height of the evaporator may produce weak turbulence in the local flow field, the turbulence effect must be considered. With the Low Re k-ε turbulence model, the turbulence variables are solved in the whole domain down to the walls and thus provide accurate input values for the transport equations. Using the assumption that the velocity and pressure field are independent of the air temperature and moisture content makes it possible to calculate the turbulent flow field in advance and then use it as input for the species transport equations.

The initial ambient relative humidity is 40% (refer to the local average air humidity for a month). The water evaporates on the surface of the evaporator, and the evaporative flux at the surface is

$$g_{evap} = K(c_{sat} - c_v)M_v \quad (27)$$

$$c_{sat} = p_{sat}/(R_g T) \quad (28)$$

The evaporation rate $K$, the molar mass of water vapor $M_v$, the vapor concentration $c_v$ and the saturation concentration $c_{sat}$ which can be calculated from the correlation. The transport equation again uses the turbulent flow field as input. Turbulence must also be considered for the diffusion coefficient, by adding the following turbulent diffusivity to the diffusion tensor:

$$\mathbf{D}_T = \nu_T \cdot \mathbf{I}/S_{cT} \quad (29)$$

where $\nu_T$ is the turbulent kinematic viscosity, $S_{cT}$ is the turbulent Schmidt number, and $\mathbf{I}$ the unit matrix. According to the above established parameters, the result of air turbulence caused by the evaporator can be obtained by solving the Navier-Stokes equation.

$$\rho(\mathbf{u}\cdot\nabla)\mathbf{u} = \nabla\cdot[-p\mathbf{I} + (\mu+\mu_T)(\nabla\mathbf{u} + (\nabla\mathbf{u})^T)] + \mathbf{F}, \quad \rho\nabla\cdot\mathbf{u} = 0, \quad (30)$$

$$\rho(\mathbf{u}\cdot\nabla)k = \nabla\cdot[(\mu+\mu_T/\sigma_k)\nabla k]+p_k-\rho\mathcal{E} \quad (31)$$

$$\rho(\mathbf{u}\cdot\nabla)\mathcal{E} = \nabla\cdot[(\mu+\mu_T/\sigma\varepsilon)\nabla\varepsilon]+c_{\varepsilon 1}(\mathcal{E}/k)p_k-c_{\varepsilon 2}\rho(\mathcal{E}^2/k)f_\varepsilon(\rho,\mu,k,\mathcal{E},l_w), \ \mathcal{E}=ep, \quad (32)$$

$$\nabla G\cdot\nabla G+\sigma_w G(\nabla\cdot\nabla G) = (1+2\sigma_w)G^4, \quad (33)$$

Where k is turbulent kinetic energy, G is reciprocal wall distance, and ep is turbulence dissipation rate, other parameters are the model parameters referenced from the software's default values. The **Figure S16** shows the distribution of the air turbulence field of evaporators at different heights in the air domain. The increase in the height of the evaporator expands more MCPR-air interfaces and greatly enhances air turbulence, leading to a dramatic increase in the flow velocity above the evaporator. According to Bernoulli's principle,

$$p+0.5\rho v^2+\rho gh = C \quad (34)$$

Where $p$ is pressure at a point in the fluid, $v$ is flow velocity at the point, $\rho$ is fluid density, $g$ is gravitational acceleration, $h$ is the height of the point and $C$ is constant. The momentum between the inside and outside of the evaporator in the same flow field conforms to Equation 29.

$$p_{in}+0.5\rho v^2\ in+\rho gh_{in} = p_{out}+0.5\rho v^2\ out+\rho gh_{out} \quad (35)$$

Where $p_{in}$, $v_{in}$ and $h_{in}$ represent the steam pressure, flow velocity and height within the evaporator domain, respectively. The $p_{out}$, $v_{out}$ and $h_{out}$ represent the steam pressure, flow velocity and height outside the evaporator domain, respectively. The increase in the height of the evaporator makes the internal gas pressure significantly higher than the outside, which helps to promote the outward diffusion of steam.

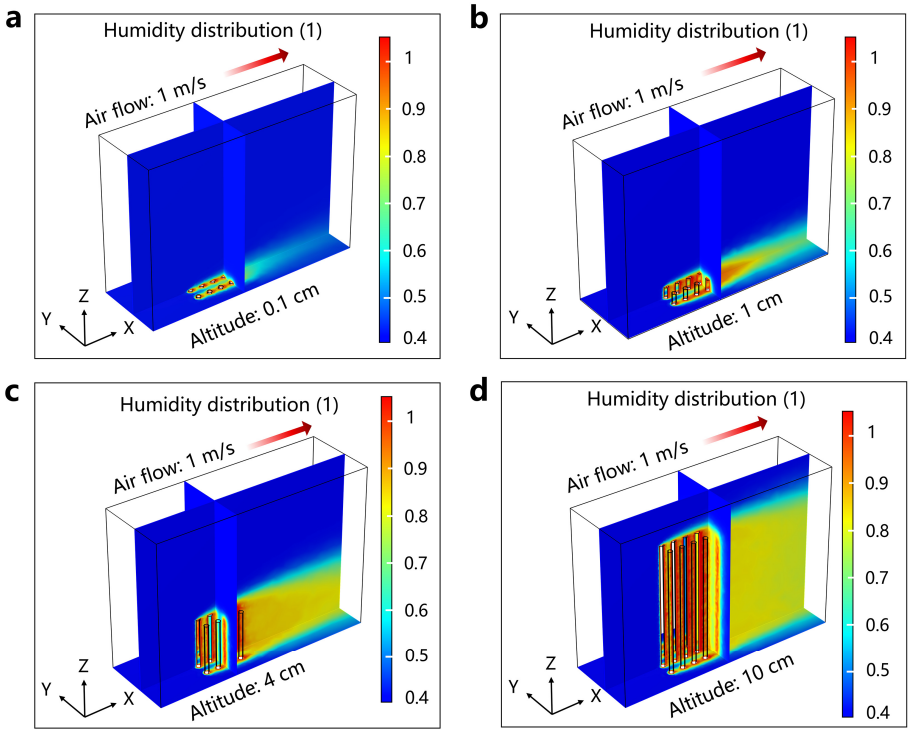


**Figure S17. Effect of evaporators with different heights on air humidity. (a)** Altitude 0.1cm. **(b)** Altitude 1 cm. **(c)** Altitude 4 cm. **(d)** Altitude 10 cm.

The influence of the evaporator with different heights on the moisture transport in the air is simulated based on the calculation result of the turbulence field.

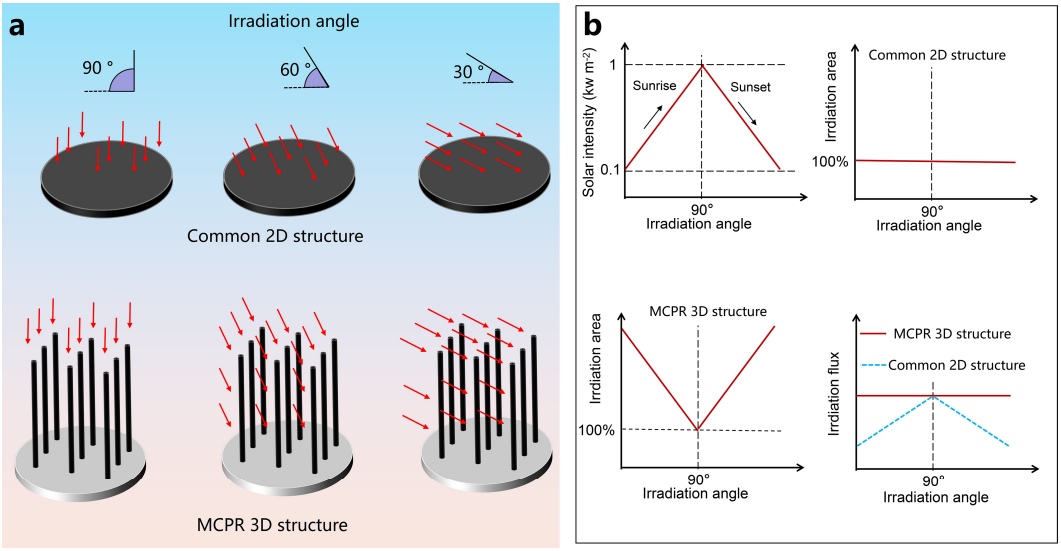


**Figure S18. Schematic diagram of the effect of radiation angle on the evaporator of the MCPR and common 2D structure. (a)** Schematic diagram showing that MCPR array increases oblique incident light-receiving area relative to common 2D structures**. (b)** The dependence of irradiation intensity and irradiation area on irradiation flux.

It can be clearly seen from **Figure S18a** that as the irradiation angle changes, the irradiation area of the common 2D structure does not significant change, but the irradiation area of the MCPR 3D structure can change with the irradiation angle. As shown in **Figure S18b**, the intensity of solar radiation varies with sunrise-sunset at different angles. The irradiation area of the common 2D structure does not change with the irradiation angle, but the irradiation area of the MCPR 3D structure can be passively adjusted according to the irradiation angle. Since the irradiated flux per unit time is equal to the irradiated intensity multiplied by the irradiated area, when the solar radiation intensity decreases, the radiation flux obtained by the common 2D structure decreases, resulting in a decrease in the evaporation efficiency. However, the MCPR 3D structure can passively increase the irradiated area when the irradiated intensity is reduced, and maintain the stability of the irradiated flux, resulting in high evaporation efficiency.

**Table S3**

**Pumping Static Height Calculation**

The equilibrium height to which water will rise within the MCPR was calculated. First, we should consider the MCPR as a system of connected micro-capillaries. The system is mainly composed of two parts, one part is composed of capillary tubes with different diameters of vertical channel (**Figure S5**), and the other part is mainly the occluded tissue wall. Since the water pumping efficiency of the capillary is significantly higher than that of the occluded tissue wall structure, in order to achieve an equilibrium height, the tissue wall structure needs to balance the weight of the rising liquid in the capillary. Therefore, the capillary tube bears the main pumping capacity, and the tissue wall structure balances the liquid height of the system through connected micro-capillaries. The equilibrium height $h$ of MCPR can be obtained by balancing the weight of the liquid that has ascended in these different channels with the surface tension force experienced by the ascended liquid column.

$$\gamma(2\pi R)cos\theta = h\rho g\pi R^2 \quad (36)$$

Here, due to the contact is extremely hydrophilic so that the contact angle $\theta$ made by the rising water meniscus inside the MCPR capillaries is very small. In the equation (30), γ is the water surface tension and $\rho$ is the density of water. We can extend this idea to our MCPR system, which consists of a total of $N$ number of channels of $k$ different radii ($R_1$, $R_2$,….$R_k$). The number of each channel is $n_1$, $n_2$,.....$n_k$, respectively. Therefore, the number density of the channels can be denoted as $x_1$, $x_2$,….$x_k$ (where $x_j=n_j/N$). Under this condition, equation (37) may be employed to calculate the height $h$ as:

$$h = 2\gamma\sum^{k}_{i=1}x_iR_i/(\rho g\sum^{k}_{i=1}x_iR_i^2) \quad (37)$$

For this work, **Table S3** and **Figure S6** provides the distribution of MCPR microcapillaries with different dimensions.

**Table S3. Distribution of radii for the MCPR channels.**

| R (microns) | Frequency ($n_i$) | $x_i=n_i/\sum n_i$ |
|---|---|---|
| 1<=R<5 | 15512 | 0.840895539 |
| 5<=R<10 | 2114 | 0.114598580 |
| 10<=R<15 | 378 | 0.020491137 |
| 15<=R<20 | 119 | 0.006450913 |
| 20<=R<25 | 105 | 0.005691982 |
| 25<=R<30 | 91 | 0.004933051 |
| 30<=R<50 | 73 | 0.003957283 |
| 50<=R<100 | 36 | 0.001951537 |
| 100<=R<150 | 19 | 0.001029978 |

The values in **Table S3** were plugged into equation (37) to obtain the equilibrium height: $h$ = 97.4 cm. However, the equilibrium height cannot be used as the actual evaporation height. According to the Lucas-Washbum equation (38), the distance of liquid diffusion is proportional to the diffusion time.

$$D^2 = (\gamma r \cos\theta t)/(2\mu) \quad (38)$$

Where D is distance of liquid diffusion, $\gamma$ is surface tension coefficient, r is pore radius, $\theta$ is contact angle, t is diffusion time and $\mu$ is hydrodynamic viscosity. In order to ensure that the liquid can quickly infiltrate the MCPR, the actual use height should be much lower than the equilibrium height.

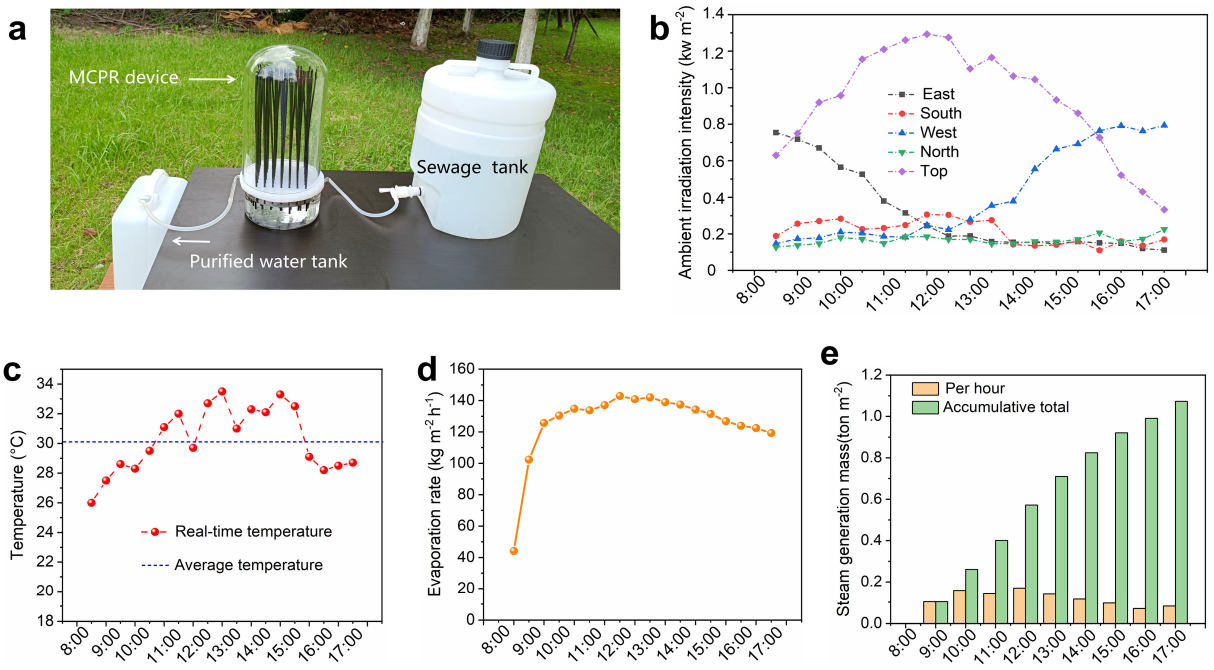


**Figure S19. Magnified MCPR evaporator produces fresh water from actual municipal sewage. (a)** Photograph showing the purification of municipal sewage in outdoor environment. **(b)** Irradiation intensities at the directions of east, south, west, north, and top, respectively. **(c)** Real-time ambient temperature at different time (from 8:00 to 17:00). **(d)** The rate of evaporation over time. **(e)** The accumulated steam mass.

*According to the analysis in **Table S3,** we constructed a large-scale integrated MCPR evaporator with an effective evaporation height-35 cm for sewage purification. Evaporation rates were evaluated in open systems and condensate yields were obtained in closed systems.

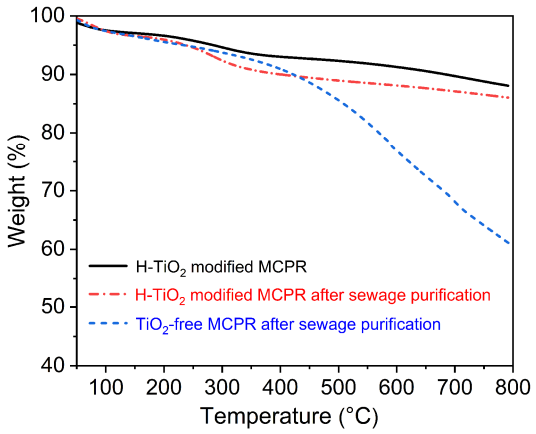


**Figure S20. Thermogravimetric data of $TiO_2$-free MCPR and H-$TiO_2$ modified MCPR.** After evaporative disposal of one liter of the municipal sewage, H-$TiO_2$ modified MCPR showed a weight loss of 14.7% at 800 °C (red dotted line), almost the same as the one not undergoing sewage disposal (black solid line). By contrast, the weight loss of $TiO_2$-free MCPR reached 39% under the same conditions (blue dotted line).

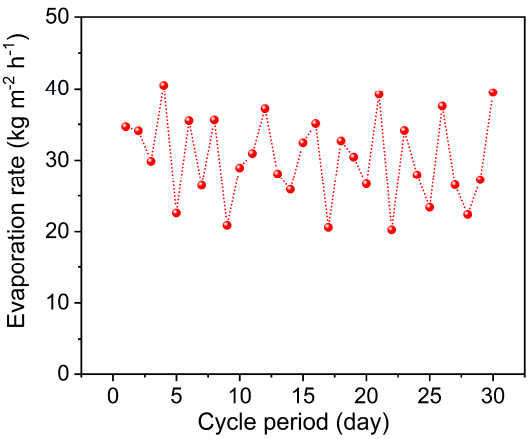


**Figure S21. Long-term evaporation performance of MCPR system under outdoor conditions.**

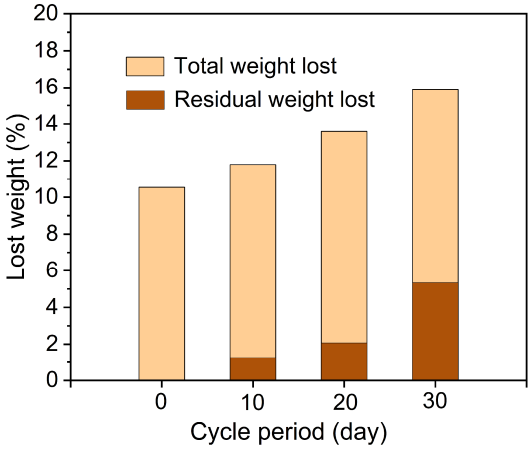


**Figure S22. Long-term photodegradation performance of MCPR system under outdoor conditions.**

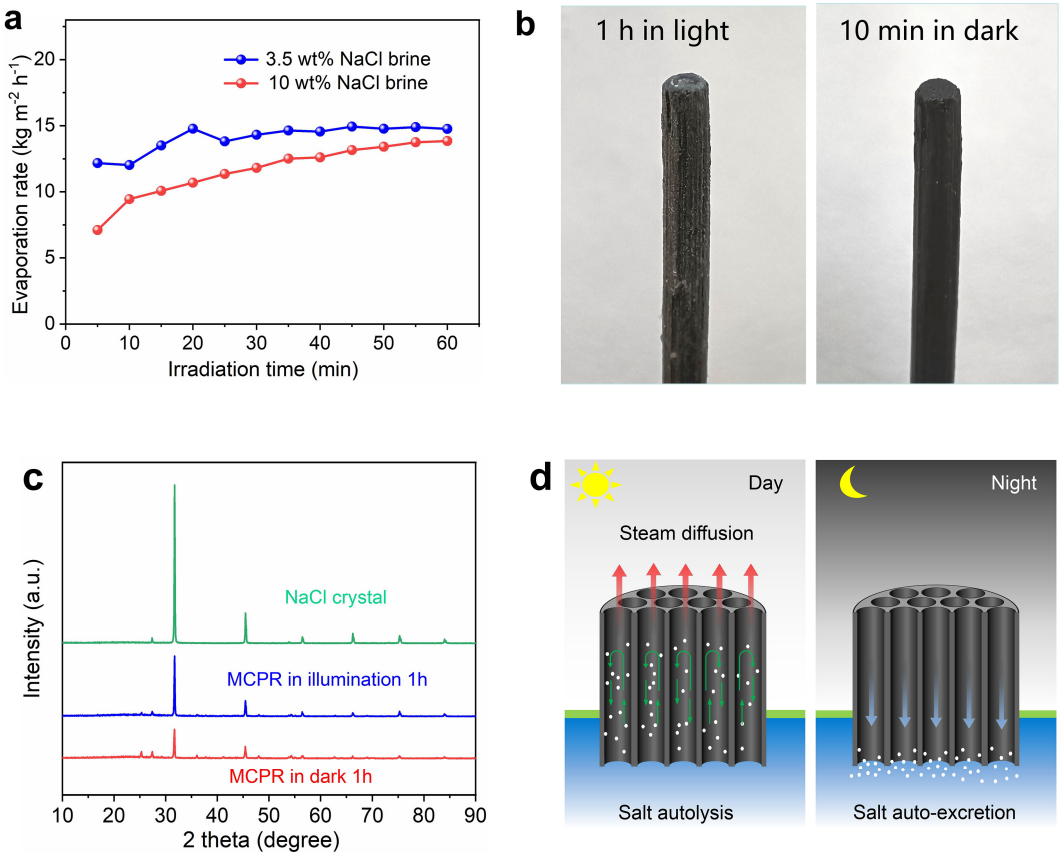


**Figure S23. Evaluation of salt resistance of MCPR system. (a)** Evaporation performance of MCPR device in 3.5wt% and 10wt% NaCl solution under 1 sun. **(b)** The MCPR was irradiated in 10 wt% NaCl brine for 1 h, and then placed in the dark for 10 min. **(c)** Changes of NaCl in MCPR before and after irradiation. Part of the salt accumulation occurred at the top of MCPR irradiated in 10 wt% NaCl brine for 1 h, and then the accumulated salt was dissolved after the illumination was stopped for 10 min. The salt reduction can also be confirmed from the XRD results. **(d)** Schematic diagram of large vertical pores produces salt autolysis and salt auto-excretion ability.

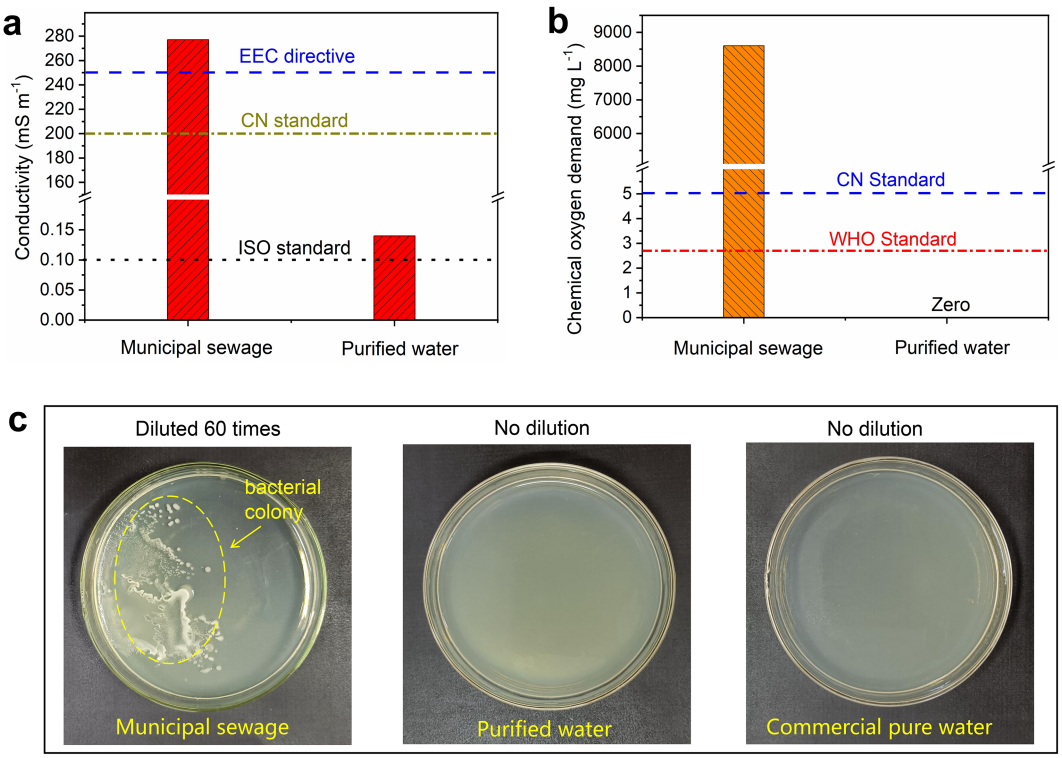


**Figure S24. Water quality assessment of the freshwater produced from municipal sewage**. **(a)** Comparison of the conductivity of the sewage and the purified water. **(b)** Comparison of COD in the sewage and the purified water. **(c)** Optical photographs of Escherichia coli culture experiments on agar substrate.

**Note S1.**

The microscopic morphology of the MCPR was observed by scanning electron microscope (S-4800, HITACHI) and transmission electron microscope (FEI Tecnai G2 F20, USA).

The data collection of Movie S2 was obtained by a contact angle measuring instrument (Shanghai zhongchen digital technic apparatus co.,lt, JC2000D1), and the liquid used was water.

The specific surface area and pore size distribution of the MCPR are obtained by an ASAP3020 instrument (Micromertics, America).

The conductivity of sewage and treated water is measured by a DDS-307A conductivity meter (Shanghai INESA, China).

The chemical oxygen demand is measured by first mixing the sample to be tested and the preset reagents, and then holding it on a GL-16K multi-functional rapid digestion instrument (Glkrei instrument, China) at 165 ℃ for 20 min, and then measuring the colorimetric degree on a GL-200 multi-parameter water quality analyzer (Glkrei instrument, China).

The structure information of the sample was tested by an XRD-7000 (Shimadzu, Japan). The thermogravimetric data of the MCPR samples were characterized by a thermal analyzer (TA Q50, USA) under a nitrogen atmosphere.

An UV-Vis-NIR spectrometer (Cary-5000, Agilent) tested the light reflection of the MCPR at a wavelength of 200 to 2000 nm.

The water vapor diffusion data of the MCPR is obtained by placing the MCPR in a closed container (volume 4000 $cm^3$) and inserting a split temperature-hygrometer (AS847, Smart sensor) on the top.

The microbiological index of the water sample was obtained by the spread plate method. The Luria-Bertani medium added with agar is heated and melted, then cooled to 60~70 ℃ and poured into a sterilized petri dish, and then a sterile plate is obtained after cooling. Then take 0.05 ml of the water sample to be tested and spread it evenly on the surface of the culture medium, and let it stand for 5 min at room temperature. After condensing, turn it upside down and incubate at 37 °C for 15 h.

**Supporting References**


1. Jia, J. et al. Fabrication of bilayered attapulgite for solar steam generation with high conversion efficiency. *Chem. Eng. J.* **361**, 999-1006 (2019).
2. Qiu, P. et al. Porous three-dimensional carbon foams with interconnected microchannels for high-efficiency solar-to-vapor conversion and desalination. *J. Mater. Chem. A* **7**, 13036-13042, (2019).
3. Huang, Z. et al. A broadband aggregation-independent plasmonic absorber for highly efficient solar steam generation. *J. Mater. Chem. A* **8**, 10742-10746 (2020).
4. Huang, W. et al. Three-dimensional hierarchical CuxS-based evaporator for high-efficiency multifunctional solar distillation. *Nano Energy* **69**,104465 (2020).
5. Xu, W. et al. Efficient water transport and solar steam generation via radially, hierarchically structured aerogels. *ACS Nano* **13**, 7930-7938 (2019).
6. Zhou, X., Zhao, F., Guo, Y., Zhang, Y. & Yu, G. A hydrogel-based antifouling solar evaporator for highly efficient water desalination. *Energy Environ. Sci.* **11,** 1985-1992 (2018).
7. Xingyi, Z., Fei, Z., Youhong, G., Brian, R. & Guihua, Y. Architecting highly hydratable polymer networks to tune the water state for solar water purification. *Sci. Adv.* **5**, eaaw5484 (2019).
8. Wu, L. et al. Highly efficient three-dimensional solar evaporator for high salinity desalination by localized crystallization. *Nat. Commun*. **11**, 521 (2020).
9. Zhao, F. et al. Highly efficient solar vapour generation via hierarchically nanostructured gels. *Nat Nanotechnol.* **13**, 489-495 (2018).
10. Wang, H. et al. Artificial trees inspired by monstera for highly efficient solar steam generation in both normal and weak light environments. *Adv. Funct. Mater.* **30**, 2005513 (2020).
11. Liu, Z. et al. Continuously producing water steam and concentrated brine from seawater by hanging photothermal fabrics under sunlight. *Adv. Funct. Mater*. **29**, 1905485 (2019).
12. Yang, F. et al. Ni-based plasmonic/magnetic nanostructures as efficient light absorbers for steam generation. *Adv. Funct. Mater*. **31**, 2006294 (2020).
13. Hu, R. et al. A Janus evaporator with low tortuosity for long-term solar desalination. *J. Mater. Chem. A* **7**, 15333-15340 (2019).
14. Geng, Y. et al. Bioinspired fractal design of waste biomass-derived solar - thermal materials for highly efficient solar evaporation. *Adv. Funct. Mater.* **31**, 2000202 (2020).
15. Lee, J. et al. Macroporous photothermal bilayer evaporator for highly efficient and self-cleaning solar desalination. *Nano Energy* **77**, 105130 (2020).
16. Tu, C. et al. A 3D-Structured Sustainable Solar-Driven Steam Generator Using Super-Black Nylon Flocking Materials. *Small* **15**, e1902070, (2019).
17. Guo, Y. et al. Solar-driven all-in-one interfacial water evaporator based on electrostatic flocking. *Adv. Sustain. Syst.* **5**, 2000202 (2020).
18. Li, C. et al. Scalable and robust bilayer polymer foams for highly efficient and stable solar desalination. *Nano Energy* **60**, 841-849, (2019).
19. Wang, Y. et al. Improved light-harvesting and thermal management for efficient solar-driven water evaporation using 3D photothermal cones. *J. Mater. Chem. A* **6**, 9874-9881, (2018).
20. Shi, Y. et al. Solar evaporator with controlled salt precipitation for zero liquid discharge desalination. *Environ. Sci. Technol.* **52**, 11822-11830 (2018).
21. Song, H. et al. Cold vapor generation beyond the input solar energy limit. *Adv. Sci.* **5**, 1800222, (2018).
22. Kuang, Y. et al. A high-performance self-regenerating solar evaporator for continuous water desalination. *Adv. Mater.* **31**, e1900498, (2019).

23. Yu, Z., Cheng, S., Li, C., Li, L. & Yang, J. Highly efficient solar vapor generator enabled by a 3D hierarchical structure constructed with hydrophilic carbon felt for desalination and wastewater treatment. *ACS Appl. Mater. Interfaces.* **11**, 32038-32045 (2019).
24. Xia, Y. et al. Spatially isolating salt crystallisation from water evaporation for continuous solar steam generation and salt harvesting. *Energy Environ. Sci.* **12**, 1840-1847 (2019).
25. Xu, N. et al. Mushrooms as efficient solar steam-generation devices. *Adv. Mater.* **29**, 1606762 (2017).
26. Zhang, Q. et al. Vertically aligned juncus effusus fibril composites for omnidirectional solar evaporation. *Carbon* **156**, 225-233 (2020).
27. Li, J. et al. Over 10 kg $m^{-2}$ $h^{-1}$ evaporation rate enabled by a 3D interconnected porous carbon foam. *Joule* **4**, 928-937 (2020).
28. Wang, H., Zhang, R., Yuan, D., Xu, S. & Wang, L. Gas foaming guided fabrication of 3D porous plasmonic nanoplatform with broadband absorption, tunable shape, excellent stability, and high photothermal efficiency for solar water purification. *Adv. Funct. Mater.* **30**, 202003995 (2020).
29. Ni, F. et al. Micro-/macroscopically synergetic control of switchable 2D/3D photothermal water purification enabled by robust, portable, and cost-effective cellulose papers. *ACS Appl. Mater. Interfaces* **11**, 15498-15506 (2019).
30. Wang, Y. et al. Boosting solar steam generation by structure enhanced energy management. *Sci. Bull.* **65**, 1380-1388 (2020).
31. Y. Tian, X. Liu, S. Xu, J. Li, A. Caratenuto, Y. Mu, Z. Wang, F. Chen, R. Yang, J. Liu, M.L. Minus, Y. Zheng, Recyclable and efficient ocean biomass-derived hydrogel photothermal evaporator for thermally-localized solar desalination, *Desalination* **523**,115449 (2022).
32. B. Lv, C. Gao, Y. Xu, X. Fan, J. Xiao, Y. Liu, C. Song, A self-floating, salt-resistant 3D Janus radish-based evaporator for highly efficient solar desalination, *Desalination* **510**,115093 (2021).
33. Y. Yang, W. Fan, S. Yuan, J. Tian, G. Chao, T. Liu, A 3D-printed integrated MXene-based evaporator with a vertical array structure for salt-resistant solar desalination, *Journal of Materials Chemistry A* **9**, 23968-23976 (2021) .
34. T. Gao, X. Wu, Y. Wang, G. Owens, H. Xu, A Hollow and Compressible 3D Photothermal Evaporator for Highly Efficient Solar Steam Generation without Energy Loss, *Solar RRL* **5**,2100053 (2021).
35. Z. Huang, Y.H. Luo, W.Y. Geng, Y. Wan, S. Li, C.S. Lee, Marriage of 2D Covalent-Organic Framework and 3D Network as Stable Solar-Thermal Still for Efficient Solar Steam Generation, *Small Methods* **5**, e2100036 (2021) .
36. C. Zhang, B. Yuan, Y. Liang, L. Yang, L. Bai, H. Yang, D. Wei, W. Wang, H. Chen, Solar vapor generator: A natural all-in-one 3D system derived from cattail, *Solar Energy Materials and Solar Cells* **227**, 11127 (2021).
37. X. Liu, Y. Tian, F. Chen, A. Caratenuto, J.A. DeGiorgis, M. Elsonbaty, Y. Wan, R. Ahlgren, Y. Zheng, An Easy-to-Fabricate 2.5D Evaporator for Efficient Solar Desalination, *Advanced Functional Materials* **31**,2100911 (2021).
38. P. Cao, L. Zhao, J. Zhang, L. Zhang, P. Yuan, Y. Zhang, Q. Li, Gradient Heating Effect Modulated by Hydrophobic/Hydrophilic Carbon Nanotube Network Structures for Ultrafast Solar Steam Generation, *ACS Appl. Mater. Interfaces* **13**, 19109-19116 (2021) .
39. H. Li, W. Zhu, M. Li, Y. Li, R.T.K. Kwok, J.W.Y. Lam, L. Wang, D. Wang, B.Z. Tang, Side Area-Assisted 3D Evaporator with Antibiofouling Function for Ultra-Efficient Solar Steam Generation, *Adv. Mater*. **33**, e2102258(2021) .
40. Y. Peng, S. Tang, X. Wang, R. Ran, A High Strength Hydrogel with a Core–Shell Structure Simultaneously

Serving as Strain Sensor and Solar Water Evaporator, *Macromolecular Materials and Engineering* **306**,2100309 (2021).

41. Z. Xie, J. Zhu, L. Zhang, Three-Dimensionally Structured Polypyrrole-Coated Setaria viridis Spike Composites for Efficient Solar Steam Generation, *ACS Appl. Mater. Interfaces* **13**, 9027-9035(2021) .
42. S. Wang, H. Deng, H. Chang, Y. Li, H. Hui, Z. Dong, P. Pu, Co-Hydrothermal Carbonization of Cotton Stalks and MnO2 for Direct Solar Steam Generation with High Efficiency, *Solar RRL* (2021).
43. X. Wang, Z. Li, Y. Wu, H. Guo, X. Zhang, Y. Yang, H. Mu, J. Duan, Construction of a Three-Dimensional Interpenetrating Network Sponge for High-Efficiency and Cavity-Enhanced Solar-Driven Wastewater Treatment, *ACS Appl. Mater. Interfaces* **13**,10902-10915 (2021).
44. Y. Lu, D. Fan, Y. Wang, H. Xu, C. Lu, X. Yang, Surface Patterning of Two-Dimensional Nanostructure-Embedded Photothermal Hydrogels for High-Yield Solar Steam Generation, *ACS Nano* **15**, 10366-10376(2021).
45. X. Chen, N. Yang, Y. Wang, H. He, J. Wang, J. Wan, H. Jiang, B. Xu, L. Wang, R. Yu, L. Tong, L. Gu, Q. Xiong, C. Chen, S. Zhang, D. Wang, Highly Efficient Photothermal Conversion and Water Transport during Solar Evaporation Enabled by Amorphous Hollow Multishelled Nanocomposites, *Adv. Mater.* e2107400 (2021).
46. X. Sun, X. Jia, J. Yang, S. Wang, Y. Li, D. Shao, H. Song, Bamboo fiber-reinforced chitosan sponge as a robust photothermal evaporator for efficient solar vapor generation, *Journal of Materials Chemistry A* **9**, 23891-23901(2021).
47. W. Zhang, Q. Chang, C. Xue, J. Yang, S. Hu, A Gelation-Stabilized Strategy toward Photothermal Architecture Design for Highly Efficient Solar Water Evaporation, *Solar RRL* 2100133(2021).
48. Y. Liang, Y. Bai, A.-Q. Xie, J. Mao, L. Zhu, S. Chen, Solar-Initiated Frontal Polymerization of Photothermic Hydrogels with High Swelling Properties for Efficient Water Evaporation, *Solar RRL* 2100917(2021).
49. C. Wei, X. Zhang, S. Ma, C. Zhang, Y. Li, D. Chen, H. Jiang, Z. Xu, X. Huang, Ultra-robust vertically aligned three-dimensional (3D) Janus hollow fiber membranes for interfacial solar-driven steam generation with salt-resistant and multi-media purification, *Chemical Engineering Journal* **425,**130118 (2021).
50. D. Xie, M. He, X. Li, J. Sun, J. Luo, Y. Wu, F. Cheng, Tree-inspired efficient solar evaporation and simultaneous in-situ purification of ultra-highly concentrated mixed volatile organic wastewater, *Nano Energy* **93**,106802 (2022).
51. Y. Li, X.-l. Shi, L.-j. Sun, M. Zhao, T. Jiang, W. Jiang, M. Deng, S. Yang, Y. Wang, Composite hydrogel-based photothermal self-pumping system with salt and bacteria resistance for super-efficient solar-powered water evaporation, *Desalination* **515**,115192 (2021).
52. Y. Tian, X. Liu, Z. Wang, A. Caratenuto, F. Chen, Y. Wan, Y. Zheng, Carbonized cattle manure-based photothermal evaporator with hierarchically bimodal pores for solar desalination in high-salinity brines, *Desalination* **520**,115345 (2021).
53. Y. Tian, X. Liu, J. Li, Y. Deng, J.A. DeGiorgis, S. Zhou, A. Caratenuto, M.L. Minus, Y. Wan, G. Xiao, Y. Zheng, Farm-waste-derived recyclable photothermal evaporator, *Cell Reports Physical Science* **2**,100549 (2021).
54. Zhou, J. et al. Development and Evolution of the System Structure for Highly Efficient Solar Steam Generation from Zero to Three Dimensions. *Advanced Functional Materials* **29**, 1903255 (2019).
55. Mu, X. et al. Strategies for breaking theoretical evaporation limitation in direct solar steam generation. *Solar Energy Materials and Solar Cells* **220**, 110842 (2021).
56. Li, X.,et al. Measuring conversion efficiency of solar vapor generation. *Joule* **3**, 1798-1803. (2019).

57. Moran, M. J., Shapiro, H. N., Boettner, D. D., Bailey, M. B. (John Wiley & Sons, 010). Fundamentals of engineering thermodynamics.